INFLUENCE OF AN-/DIHEDRAL AND OF DIFFERENT BLADE SHAPES ON PERFORMANCE AND AEROACOUSTICS OF AN ISOLATED ROTOR

Martin Hollands, Manuel Keßler, Ewald Krämer
hollands@iag.uni-stuttgart.de
IAG University of Stuttgart, Pfaffenwaldring 21,70569 Stuttgart, Germany

Abstract

In the present study different blade shape designs are evaluated in forward flight and hover condition to improve the performance of the helicopter rotor. In particular the effect of introducing an-/dihedral and a variation of the chord length is examined. Anhedral has a positive effect on hover performance while dihedral is of advantage in forward flight. Increased chord length shows benefits in forward flight within a broad range of its parameters radial position and size of the chord length. Finally, the noise emission is evaluated for several promising blade shapes in an ICAO $6°$-descent flight condition. The examined blade shapes differ only slightly in their acoustic properties.

NOMENCLATURE

μ	rotor advance ratio	[-]
Ψ	Rotor azimuth angle	[°]
σ	rotor solidity	[-]
θ_0	Collective pitch angle	[°]
θ_C	Cyclic pitch angle (cosine)	[°]
θ_S	Cyclic pitch angle (sine)	[°]
$\vec{F}_{2D}$	Aerodynamic blade sectional loads and moments vector (BET)	
$\vec{F}_{3D}$	Aerodynamic blade sectional loads and moments vector (CFD)	
C_P	Power coefficient of the rotor	$[-]$
C_Q	Sectional torque coefficient $C_Q = Q_r/(\rho\pi R(\Omega R)^2 R)$	$[-]$
C_T	Sectional thrust coefficient $C_T = T_r/(\rho\pi R(\Omega R)^2)$	$[-]$
FM	Figure of Merit	$[-]$
L/D	Lift over Drag ratio of the rotor	$[-]$
P	Power of the rotor	$[W]$
Q_r	Sectional torque	$[Nm/m]$
R	Rotor radius	[m]
SPL	Sound pressure level	[dB]
T_r	Sectional thrust	$[N/m]$
v_∞	Forward flight speed	$[m/s]$
X	Propulsive force of the rotor	$[N]$
ANOVA	Analysis of variance	
BET	Blade element theory	
BPF	Blade passing frequency	
BVI	Blade vortex interaction	
CFD	Computational fluid dynamics	
CSD	Computational structural dynamics	
FISUW	Finite state unsteady wake	
RANS	Reynolds-Averaged Navier-Stokes	

1 INTRODUCTION

Advanced helicopter design focuses on lower fuel consumption and reduced noise emission. Therefore, in the framework of the German research project FTEG-ECO-HC the influence of different blade geometries on the performance of a full-scale isolated rotor at high cruise speed and in hover is investigated. Additionally, aeroacoustic emission in an ICAO $6°$-descent flight condition is evaluated for promising blade shapes. In a previous study [1] a positive effect on performance was found by increasing the chord length close to the blade tip. Furthermore, anhedral showed a positive influence on hover performance whereas having a negative effect on forward flight performance. Based on this study the influence of an-/dihedral is further examined. While in the previous study the best blade showed a performance benefit of 7.6% in forward flight compared to a rectangular shaped reference blade with parabolic leading edge at the blade tip, in the present study an improvement of more than 11% is achieved by introducing a slight dihedral. Subsequently, the radial positioning as well as the size of an increased chord length is examined in a detailed study of these two parameters.

1.1 Applied Methods

The process chain for conducting parametric studies on different blade shape designs consists of several steps. At first the blade surface is parametrized, then the blade mesh is automatically generated with AutoMesh [2]. Finally aeroelastic simulations are performed with the aeromechanics code *HOST* from Eurocopter [3] and the finite volume unsteady RANS solver *FLOWer* from DLR [4]. Aeroacoustic evaluation is conducted in the ICAO 6°-descent flight condition applying the Ffowcs Williams-Hawkings solver ACCO [5]. In order to determine the relevance of different parameters and to reduce the number of computationally costly coupled CFD simulations, the effect of an-/ dihedral is examined using a Design of Experiments (DoE) approach from Taguchi [6]. A multi fidelity approach with two steps is chosen for a thorough investigation of an increased chord length. Starting with the Finite State Unsteady Wake (FISUW) model implemented in *HOST* [7] as reduced model to examine the parametric space, Computational Fluid Dynamics (CFD) calculations are performed in a second step in areas of interest.

1.1.1 Aerodynamic Modeling - (CFD)

The finite volume code *FLOWer* used in this study discretizes the unsteady Reynolds- Averaged Navier-Stokes (RANS) equations with second order central differences in space and with an implicit dual time-stepping method by Jameson [8] in time. For turbulence modeling the Wilcox $k-\omega$ model [9], and as convergence accelerators implicit residual smoothing and a multigrid method on three grid levels are applied. Independent motion definitions between different grid structures with grid deformation of the blade meshes is made possible by the Chimera technique [10].

1.1.2 Structural Modeling - (CSD)

The structural model of the rotor blade within *HOST* is an Euler-Bernoulli beam with rigid elements connected by virtual joints to realize rotations around all three axes. The multi degree of freedom system from these rigid elements is reduced with the Rayleigh-Ritz method to a modal decomposition using a limited amount of mode shapes [11].

1.1.3 Fluid Structure Coupling

The weak fluid structure coupling method [12] is used to calculate fluid-structure interaction. This method makes use of the periodicity of the examined flight conditions (hover, steady forward flight and steady descent flight), hence periodic loads and deformations are exchanged between the structural code *HOST* and the CFD solver *FLOWer*. In forward flight and descent flight condition the rotor is trimmed to meet the objectives thrust, rolling and pitching moment by adapting collective and cyclic pitch angles, while in hover the rotor is trimmed to a fixed thrust with only the collective pitch as control angle. The coupling procedure is accomplished by Python scripts. An initial deformation and trim state is calculated by *HOST* based on blade element theory. The blade deformation and control angles are transfered to *FLOWer* and the corresponding CFD solution is calculated. In the next step, loads and moments $\vec{F}^{n}_{3D}$ are transferred back to *HOST* and the deformation and control angles for the next trim iteration are determined based on sectional blade loads vector $\vec{F}^{n+1}_{HOST}$ calculated by the following equation:

$$\vec{F}^{n+1}_{HOST} = \vec{F}^{n+1}_{2D} + \left(\vec{F}^{n}_{3D} - \vec{F}^{n}_{2D}\right) \tag{1}$$

This procedure is repeated until $\vec{F}_{2D}$ is constant and $\vec{F}^{n+1}_{HOST}$ consists only of the CFD loads. In this case the control angles are also constant which serves as criterion of a converged trim. For the present simulations the trim is considered converged when the pitch angles are constant in the second decimal place.

1.1.4 Grid Generation and grid setup

AutoMesh builds multi-block structured blade meshes with constant topology and node distribution for arbitrary blade shapes. In [1], a detailed grid convergence study was conducted, evaluating the dependency of global performance criteria on three different grid levels. The error on the coarsest grid was at 2.2%, evaluated with the trim state of the finest mesh resolution. Furthermore, it was shown, that on the coarse grid, even though the accumulated error within the trim process is at 7.4% for absolute values, the coarse grid is sufficient for determining differences between various blade geometries. Provided that different rotor blades were locally resolved with the same mesh resolution, a good qualitative agreement was found comparing the solution on the coarse mesh and the next refinement level for different blade shapes. Thus, in the present study the coarse mesh setup is used for the evaluation of hover and forward flight performance. This setup uses 1.4 million cells for each blade grid and 1.6 million cells for the background mesh. The boundary layer is resolved with 28 cells, with the height of the first boundary layer cell being $y^{+} < 1$. In forward flight and descent flight the setup consists of an isolated rotor with 5 rotor blades embedded in a Cartesian background mesh. In hover a periodic setup with only one rotor blade and a 72° piece of a cylinder with periodic boundary condition is used as background mesh. For the acoustic evaluation an additional grid convergence study is performed using a highly resolved background mesh.

1.1.5 Quality criteria

In hover the Figure of Merit FM is used to evaluate the performance of different rotor blades. As a three component trim of the isolated rotor is used in forward flight condition, the performance of the rotor depends not only on the consumed power, but also on the varying propulsive force. Therefore, instead of using the power-coefficient C_P, the Lift over Drag ratio L/D is taken as quality criterion in forward flight. In [13] it is defined as:

(2) $$\frac{L}{D} = \frac{L}{\frac{P}{v_\infty} - X}$$

1.1.6 Acoustics Acoustic properties of the rotor have been studied in an ICAO 6°-descent flight condition, relevant for Blade Vortex Interaction (BVI) noise. For the calculation of the noise emission, control surfaces enveloping the rotor blades have been evaluated, applying the Ffowcs-Williams and Hawkings (FW-H) solver ACCO. The control surfaces provide the coordinates (x, y, z), the flow properties density, pressure and the velocity vector for each time step. Grid motion is calculated by first order finite differences from the movement of the point coordinates. The FW-H equation is an extension of the Lighthill analogy, allowing arbitrary motion of acoustic sources by integrating on a control surface engulfing the rotor blades, accounting for acoustic sources within these surfaces. The Lighthill analogy is limited to constant flow conditions outside the control volume. This limitation is still valid for the FW-H formulation as it uses the wave equation for propagation to the observers.

2 PERFORMANCE RESULTS

2.1 An-/ Dihedral

In an earlier study [1] an important improvement of the forward flight performance was achieved by increasing the chord length at a position of about 80% rotor radius. The average chord length was kept constant by decreasing the chord length at the blade tip. In this study, blades with a slightly downward bent blade tip (anhedral) have also been investigated. Even a slight anhedral of 8% of the reference chord length showed a considerable effect on rotor performance in hover and in forward flight. While anhedral was beneficial in hover, it showed negative effects on rotor performance in forward flight. Therefore, the influence of an-/ dihedral on forward flight and hover performance is studied here in detail. The deflection of the blade tip is parametrized with four factors (A, B, C, D), each with two levels (Figure 1, Table 1). Parameter A varies the radial position of the onset of the deflection, B represents the deflection itself (either downwards - anhedral, parameter C, level 1 or upwards - dihedral, parameter C, level 2), and finally parameter D describes the evolution of the deflection (parabolic or linear). Following the Taguchi method with an L-8 orthogonal array, the significance of the four factors can be determined. Table 2 presents the orthogonal array on the left-hand side with the level settings for the different factors for each numerical experiment.

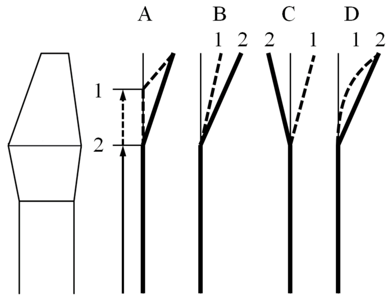

Fig. 1: Schematic of blade shapes with an-/ dihedral variation in parameters A, B, C and D

Table 1: Factor levels

	Factor	Level 1	Level 2
A	r/R	0.9464	0.875
B	Out-of-plane / cref	0.0825	0.264
C	An-/ Dihedral	Anhedral	Dihedral
D	Parabolic / Linear	Parabolic	Linear

The results for forward flight and hover are listed in two columns each, accounting for the uncertainty in the values of the quality criterion caused by the trim process. Value $(n-1)$ represents the second to the last and n the last trim iteration. The different values of an-/ dihedral have been applied to the rotor blade which served as basis for a detailed grid convergence study in [1]. This rotor blade (Figure 13 blade 2) performed well in forward flight with an $L/D = 7.139$ compared to $L/D = 6.784$ of the rectangular shaped reference blade with parabolic blade tip (Figure 13 blade 1). In hover there was a slight setback with $FM = 0.724$ compared to $FM = 0.733$ of the reference blade. In Table 2 these values can be found in the first line (Exp. 1). The results show the same trend for the blades with anhedral as in study [1], in which these blades were less efficient in forward flight but were better in hover. Introducing a dihedral to the rotor blade increases the efficiency in forward flight with a slight penalty in hover and has thus an effect contrary to anhedral. Increasing the deflection further

Table 2: Inner Array L-8

Exp	Control factor A	B	C	D	Forward flight L/D_{n-1}	L/D_n	Hover FM_{n-1}	FM_n
1	1	1	1	1	7.137	7.139	0.7245	0.7244
2	1	1	2	2	7.398	7.390	0.7135	0.7131
3	1	2	1	2	6.698	6.695	0.7336	0.7336
4	1	2	2	1	7.228	7.231	0.6904	0.6894
5	2	1	1	2	7.147	7.150	0.7223	0.7221
6	2	1	2	1	7.377	7.384	0.7145	0.7133
7	2	2	1	1	6.560	6.567	0.7221	0.7214
8	2	2	2	2	7.545	7.545	0.7073	0.7068
Reference blade					6.784		0.733	

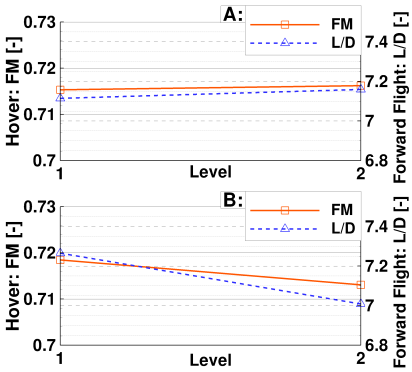

Fig. 2: Significance of factor A: radial position; B: out of plane position for hover and forward flight

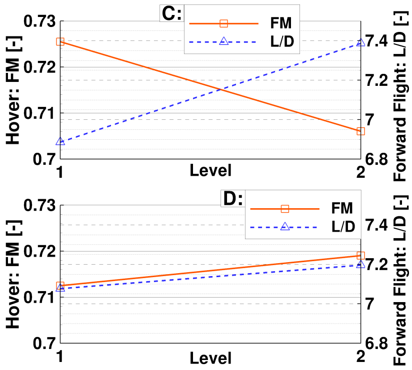

Fig. 3: Significance of factor C: an-/dihedral; D: parabolic/linear for hover and forward flight

Table 3: ANOVA results for forward flight

	DOF	Sum of squares	Mean Square	Significance p [%]
A	1	0.008	0.000	0.00
B	1	0.263	0.234	14.24
C	1	1.002	0.973	59.12
D	1	0.055	0.270	1.64
error	11	0.316		25.00
total	15	1.646		100.00

Table 4: ANOVA results for hover

	DOF	Sum of squares $[10^{-4}]$	Mean Square $[10^{-4}]$	Significance p [%]
A	1	0.026	0.000	0.00
B	1	1.163	0.574	2.34
C	1	15.153	14.565	59.41
D	1	1.702	1.114	4.55
error	11	6.471		33.70
total	15	24.518		100.00

than level 1 tends to have a negative effect both in hover and in forward flight (compare Figure 2).
The results of the analysis of variance (ANOVA) in Table 3 and 4 as well as Figures 2 and 3 show the significance of the four factors. Clearly the highest influence is found for factor C (an-/dihedral) both in hover and in forward flight. Figure 3 illustrates the contrary effect of parameter C in hover and in forward flight stated before. Looking at the variation of the an-/dihedral by the factors A, B and D, all factors act in the same direction for hover and forward flight. However, the influence of the radial position (factor A) is negligible. A moderate deflection (factor B, 1) tends to be of advantage in both flight conditions (Figure 2). In forward flight and in hover the evolution of the deflection (factor D) shows a benefit for the linear evolution (Figure 3). The optimum parameter set predicted by the Taguchi method is in forward flight (2, 1, 2, 2) with an expected value of $L/D = 7.595$, the CFD solution for this configuration is $L/D = 7.392$ and $FM = 0.717$. Thus it yields an improvement of 9% compared to the reference blade with $L/D = 6.784$, but is still worse than configuration Exp. 8 which means an enhancement of more than 11%. Nevertheless, in hover the Figure of Merit is only 2% worse than the reference blade. For hover Exp. 5 is proposed as best configuration of the parameters, yet it is 1.5% worse than the reference blade, while Exp. 3 is on an equal level with the reference blade. The offset between the optimum sets predicted by the Taguchi method and the calculated values is due to the correlation of the different parameters. Thus, additional experiments with an outer array are required to account for the correlation of the factors.

In Hover all blades with anhedral and all blades with dihedral show a similar behavior concerning thrust (C_T) and torque (C_Q) distribution along the rotor blade (Figure 4). While the blades with anhedral

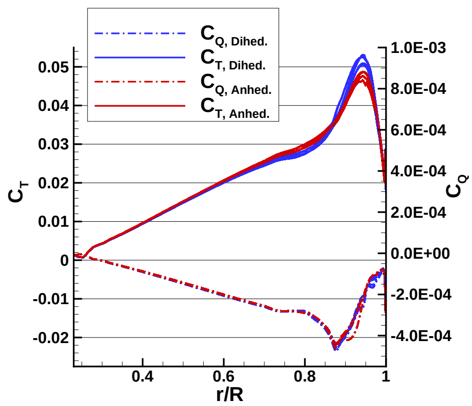

Fig. 4: An-/Dihedral: Thrust coefficient C_T and torque coefficient C_Q in hover for all 8 experiments

show a less pronounced C_T peak than blades with dihedral, there are almost no differences in the torque coefficient, except for blade Exp. 7 wich has a broader

peak towards the blade tip. Generally blades with a better Figure of Merit also tend to have a less distinct peak in thrust distribution.
In forward flight anhedral leads to an increased inflow at the blade tip for azimuth positions of $\Psi = 90^\circ - 270^\circ$, which causes an area of negative thrust on the advancing side as the local aerodynamic angle of attack gets negative (Figure 5). This effect can also be seen for the blades without anhedral, yet for blades with anhedral it covers a larger range of blade azimuth positions. Dihedral shifts the area with negative thrust to a smaller region around $\Psi = 90^\circ - 140^\circ$. In addition, the maximum amount of negative thrust is smaller for blades with dihedral. Shown exemplary in a difference plot between Exp.6 and Exp.5 (Figure 6), for Exp.6 with dihedral thrust generation is shifted radially outwards at $\Psi = 90^\circ - 270^\circ$, while there is a slight loss in the backward region. This behavior is also found for the other configurations with dihedral.

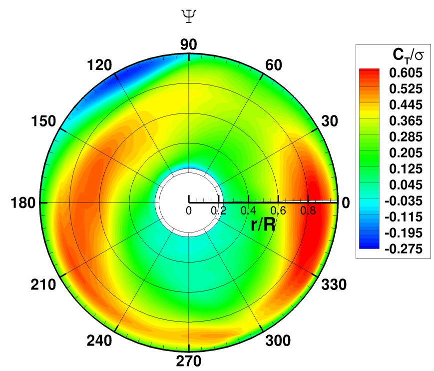

Fig. 5: Anhedral, Exp. 5: Thrust coefficient C_T in forward flight

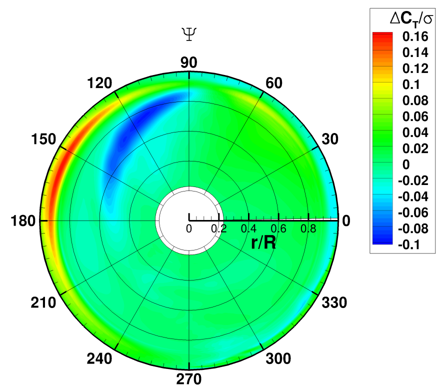

Fig. 6: [Exp 6 (dihedral) - Exp. 5 (anhedral)]: Thrust coefficient ΔC_T in forward flight

These effects are directly related to the consumed power of the rotor, as a larger area of negative thrust and radially inward shifted thrust generation require higher pitch angles (Table 5). Accordingly, the torque coefficient is also affected (Figures 7, 8 and 9). The

Table 5: Collective and cyclic pitch angles

	θ_0	θ_C	θ_S
Exp 1	4.11°	1.78°	-10.81°
Exp 2	3.84°	1.77°	-10.45°
Exp 3	4.40°	1.68°	-11.14°
Exp 4	3.61°	1.90°	-10.16°
Exp 5	4.12°	1.50°	-10.75°
Exp 6	3.82°	1.99°	-10.44°
Exp 7	4.23°	1.48°	-11.49°
Exp 8	3.48°	2.57°	-10.089°

positive values in the difference plot (Figure 8) indicate areas with reduced torque contribution of Exp. 6 (dihedral). These differences even increase, when comparing Exp. 6 with the other blades with anhedral, as Exp. 5 has the best forward flight performance among those blades with anhedral. The poor results of blade Exp. 7 in forward flight are directly related to the region around $\Psi = 270^\circ - 350^\circ$ and $r/R > 0.875$, along the deflected part of the blade (Figure 9).

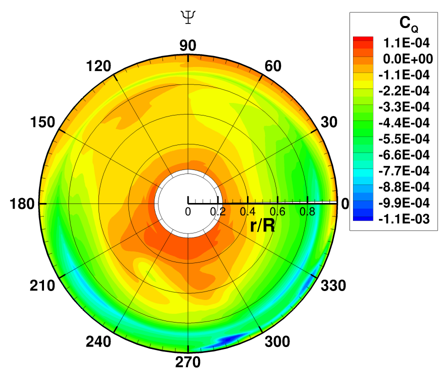

Fig. 7: Anhedral, Exp. 5: Torque coefficient C_Q in forward flight

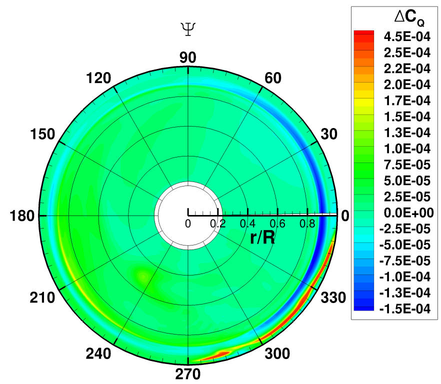

Fig. 8: [Exp 6 (dihedral) - Exp. 5 (anhedral)]: Torque coefficient ΔC_Q in forward flight

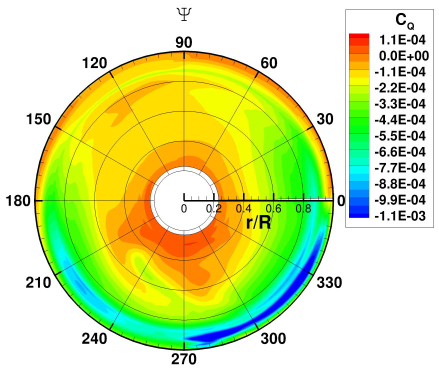

Fig. 9: Anhedral, Exp. 7: Torque coefficient C_Q in forward flight

2.2 Chord variation

In another study, two parameters are varied to examine the influence on the forward flight performance of an increased chord length in proximity of the blade tip. Figure 10 explains the two parameters chosen for the variation, *a* is the non-dimensional radial position of the largest chord length and *b* the non-dimensional chord length. Parameter *c* is adapted as a function of *a* and *b* such that blades with the same thrust-weighted average chord length are obtained. The rotor performance is analysed under fast

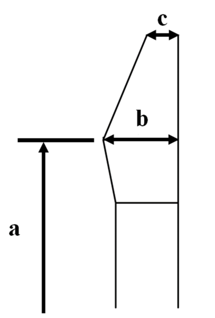

Fig. 10: Schematic of blade shapes with chord variation in parameters *a* and *b*

cruise-speed condition ($\mu = 0.36$). In a first step, the parametric area is examined with the FISUW model. As this model is based on 2D aerodynamics, the computational requirements are low and the parametric area can be resolved with several thousand points (Figure 11). While L/D shows extrema towards the borders of the parametric area, a minimum in the power coefficient C_P is present at about a=0.85, b=1.3. Based on these results fluid-structure coupled CFD simulations are performed starting at the border of the parametric domain and gathering subsequently data points around the observed C_P-optimum.

The results in Figure 12 show the evolution of the CFD calculations (marked with black filled squares). Values at empty squares were calculated by Kriging

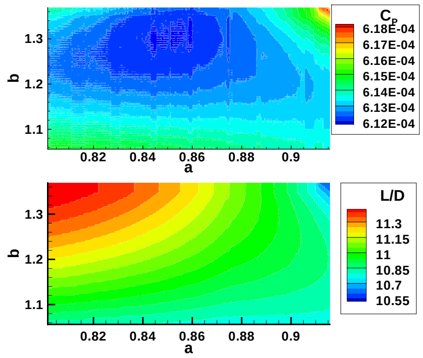

Fig. 11: Chord variation: FISUW results for C_P and L/D

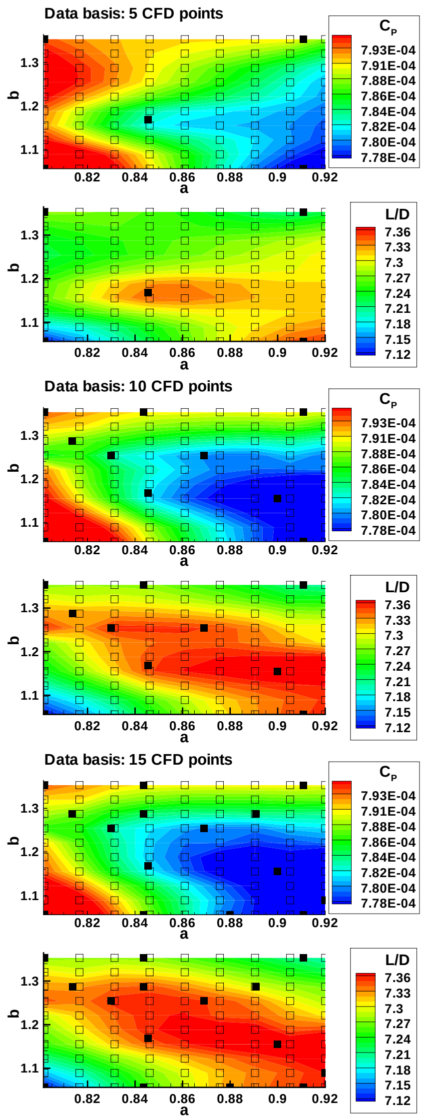

Fig. 12: Chord variation: Kriging results for C_P and L/D based on up to 15 CFD-solutions (filled squares)

interpolation. While 5 CFD solutions are not sufficient for getting an idea about the influence of the two examined parameters, with 10 CFD solutions a quite good approximation can be given. For a more detailed understanding of the parametric area 15 or more CFD solutions are required. In the area of the C_P optimum of the FISUW results, CFD results also show low power consumption, and even a good rotor performance in terms of L/D is found, which is not predicted by FISUW. The final plots based on 15 CFD points reveal a wide spread optimum, starting at $a = 0.83, b = 1.25$ and continuing with increasing radial position *a* and decreasing values for the chord length *b*. So in particular results for maximum chord positions located close to the blade tip show no accordance with the FISUW results. This is not surprising as the aerodynamic modeling does not include three dimensional effects such as the evolution of blade tip vortices and radial cross-flow. The best blade of the 15 calculated parameter sets was at $a = 0.9$, $b = 1.16$ with $L/D = 7.386$, which is a 9% improvement compared to the reference blade (Figure 13, 1).

3 ACOUSTIC RESULTS

For the acoustic evaluation the rotor is trimmed to a steady $6°$-descent flight to examine the acoustic properties of the blades related to Blade Vortex Interaction (BVI) Noise. The rectangular shaped reference blade of the current project (1), the blade Exp.1 from the previous An-/Dihedral study (2), the best solution in forward flight (3) from study [1] and finally (4) the best blade from the present chord variation study (see Figure 13) are analysed acoustically.

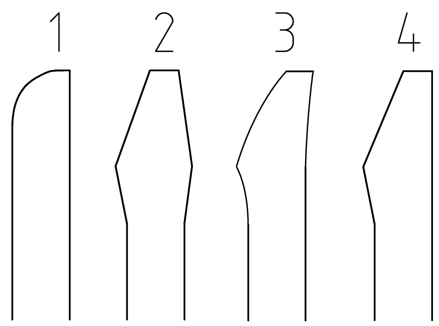

Fig. 13: Different blade shapes examined with acoustic evaluation

In order to resolve the blade tip vortices and to ensure their preservation, a background mesh with a finer mesh resolution than for the performance calculations is used. The region in proximity of the rotor blade meshes (Figure 14, small cuboids embedded with hanging grid nodes) resolve the 6^{th} blade passing frequency (BPF) with 78 and the 40^{th} BPF still with about 12 cells, resulting in a background mesh with 20 million grid points. The evolution of the blade tip vortices is visualized with the λ_2 criterion. It is possible to preserve the vortices over several rotor revolutions. The interaction of the blade tip vortices with the rotor blades on the advancing as well as on the retreating side is apparent. Concerning the blade meshes a study with three different mesh resolutions is performed, refining the blade mesh by each step with a constant factor of 1.3 in each dimension, starting with 1.4 million cells for the coarse mesh. The resolution of the background mesh is kept constant. Furthermore, the acoustic evaluation is performed on two different control surfaces. Figure 15 shows a cut through these control surfaces together with the mesh resolution of the coarse blade mesh inside the the control surface.

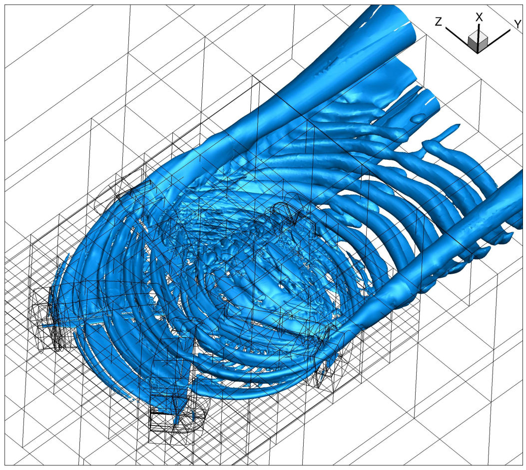

Fig. 14: λ_2 visualization of $6°$-ICAO descent flight with grid blocks

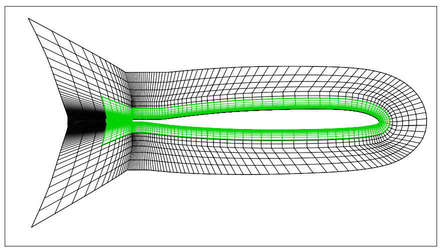

Fig. 15: Acoustic control surfaces with interior mesh resolution of the coarse blade mesh

The surfaces engulf the rotor blade and in the following will be referred to as close (Figure 15 in green) and distant control surface (in black). Corresponding surfaces (close and distant) coincide approximately for the different grid resolutions. For the coarse blade mesh the close surface is at a distance of 27 cells from the blade surface and 33 cells for the distant surface. For the intermediate grid, the surfaces are at 34 cells and 43 cells respectively and for the fine

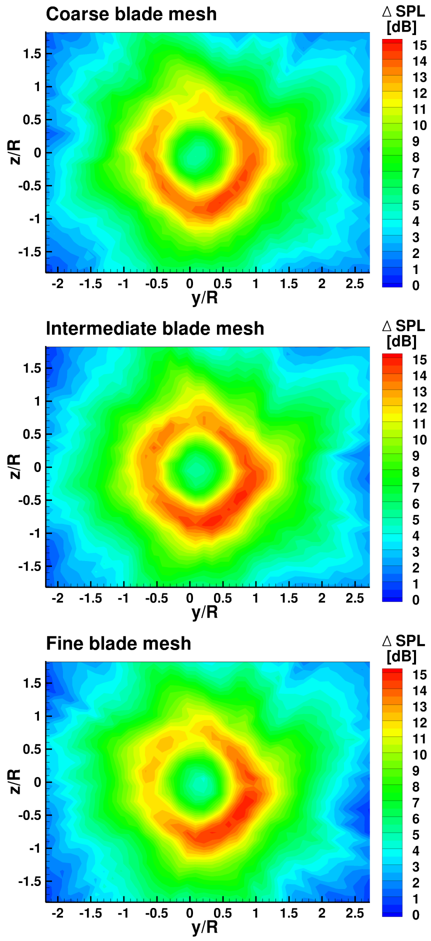

Fig. 16: SPL for close control surface on three different mesh resolutions, blade (2), flight direction to the left

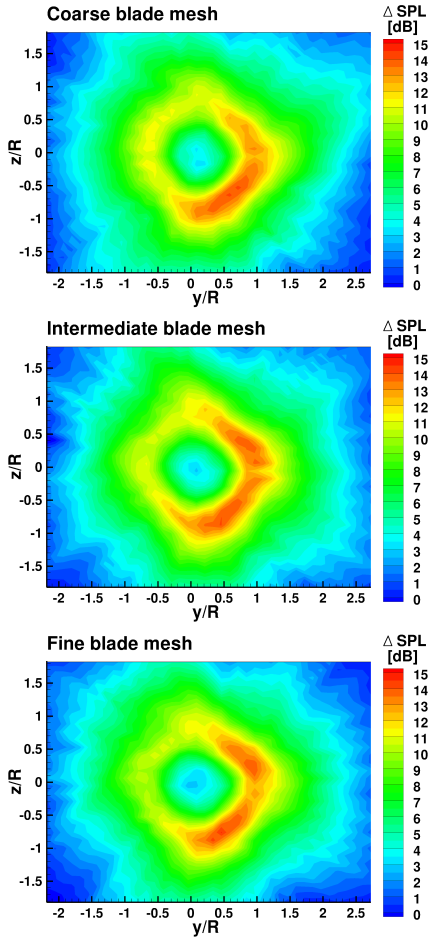

Fig. 17: SPL for distant control surface on three different mesh resolutions blade (2), flight direction to the left

mesh at 46 and 59 cells. For the acoustic evaluation a 1° timestep was chosen, so frequencies up to the 36^{th} BPF can be fully resolved. In Figures 16 and 17 an acoustic carpet one rotor radius below the rotor is presented for the different blade-mesh resolutions and the two control surfaces. The local relative differences of the sound pressure level (SPL) in $[dB]$ are plotted. The SPL-results evaluated from the close control surfaces have a circular peak region, while the distant control surfaces show two more distinct peaks on the advancing and the retreating side and have a maximum SPL which is about $0.5dB$ less for each mesh resolution. While the decrease in sound pressure level is likely to be an effect of numerical dissipation to the distant control surface, it is remarkable that increasing the mesh resolution does not lead to higher SPL values on the close control surface. Indeed, the results from the fine blade mesh and close surface resemble the results on the distant surface. The effect is likely to come from numeric disturbances due to the meshing in the wake region of the blunt trailing edge. Furthermore, as the surface is close to the boundary layer, the assumption of an undisturbed flow field outside the acoustic hull surfaces does not hold true. The dominance of this phenomenon is less apparent for the distant surface. The peaks in noise generation are located directly under the regions where a blade vortex interaction can be identified by the vortex visualization in Figure 14.

A further acoustic analysis is performed for the rectangular shaped reference blade with parabolic tip section, the best configuration in forward flight from [1] as well as the best blade from the chord variation study. All three configurations are calculated on the intermediate blade mesh with the distant control surface. While the reference blade (1) has a slightly increased maximum at the retreating blade, the optimum forward flight blade (3) shows a reduction of noise emission at the advancing side. Yet there is an increase of about $0.5dB$ at the retreating side. The blade from the chord variation study (4) shows the same characteristics as the previous blade, but there is a slight decrease of about $0.5dB$ at the retreating side. Thus the last configuration shows an overall improvement (Figure 18).

Finally, the Fast Fourier Transformed (FFT) SPL-

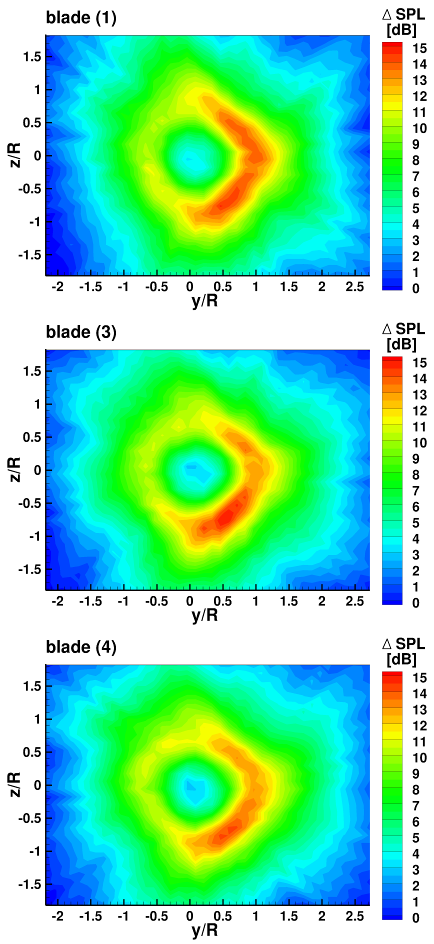

Fig. 18: SPL for distant control surface for blades (1), (3) and (4), flight direction to the left

data are presented for an observer in the peak region of the retreating blade at position ($y/R = 0.59, z/R = -0.65$). The plots (Figure 19) of the sound pressure level over the 6^{th} to 40^{th} blade passing frequency (BPF) reveal that there are non-periodic perturbations. The red line assigns the sound pressure level for multiples of the BPF and is expected to have the highest levels of the spectrum, being an envelope over the other frequencies as shown in [14]. It is found that those peaks are quite often close to a multiple of the BPF but do not coincide. Possible reasons are a not fully periodic flow field, a not sufficient temporal or spatial resolution and numeric disturbances caused by the mesh. Only the SPL of blade 2 on the fine grid evaluated on the close control surface shows in a wide area the expected behavior, yet also with non-periodic frequencies (Figure 20).

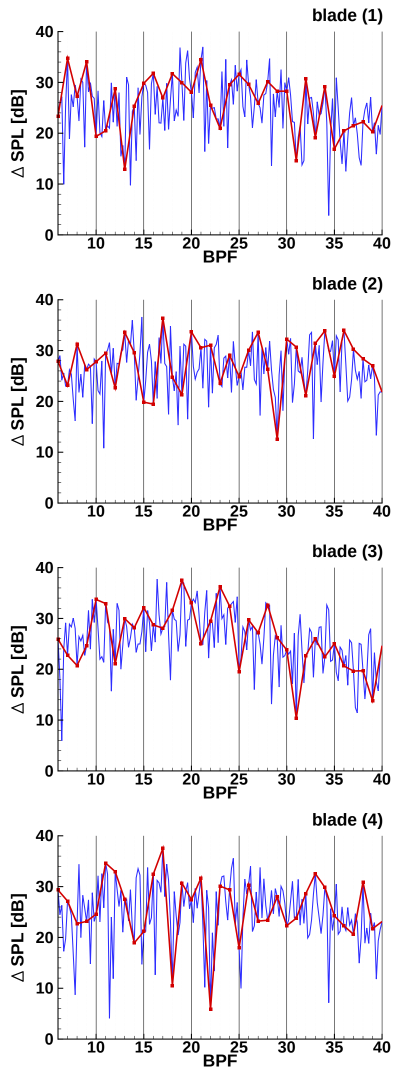

Fig. 19: Sound pressure level as function of blade passing frequency: distant surface, intermediate grid, blade (1), (2), (3), (4)

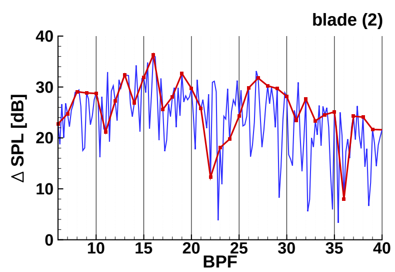

Fig. 20: Sound pressure level as function of blade passing frequency: blade 2, close surface, fine grid

4 CONCLUSION

Fluid-structure coupled CFD simulations were carried out to examine the influence of an-/dihedral on the performance of an isolated rotor in forward flight and hover. While blades with dihedral performed well in forward flight and achieved an improvement of more than 11% compared to a rectangular shaped reference blade with parabolic tip section, in hover those blades were less efficient. Blades with anhedral behaved in a contrary way. Yet the benefit of anhedral in hover was less intense than the performance loss in forward flight due to a downward deflection of the blade tip. Generally blades with a small deflection performed better both for anhedral and dihedral than those blades with a higher deflection. In another study two parameters were examined: radial position and size of an increased chord length. At first the parametric area was evaluated with a Finite State Unsteady Wake model, then CFD calculations were conducted. The necessary amount of CFD calculations was estimated to 10-15 data points to get a good idea of the behavior of the two parameters. A broad optimum range was found in the parametric area yielding an improvement of up to 9% compared to the reference blade. Finally, an acoustic evaluation of several rotor blades was performed. In a grid study the influence of grid refinement on the acoustic solution was found to be in an acceptable range for the intermediate compared to the fine mesh resolution concerning noise footprints. Larger differences occurred on the coarsest mesh resolution. Although the noise footprint of the four examined blade shapes did not show significant differences, the blade with the best performance (in terms of rotor L/D) from the present study of an increased chord length, had a reduced noise emission on the advancing side, while at the retreating side the noise level dropped only slightly. Transformation into the frequency domain showed that noise results were affected with non-periodic disturbances, likely to be caused by numerical effects or irregular flow physics, as for example unsteady separation.

Acknowledgements

The authors would like to thank the aerodynamic department of Eurocopter for their valuable input of their practical experience and the German Federal Ministry of Economy and Technology (BMWi) for its funding in the framework of FTEG-ECO-HC under grant 20H0803. We would also like to thank the members of the Helicopters and Aeroacoustics group at the IAG for their contribution.

REFERENCES

[1] Hollands, M., Keßler, M., Altmikus, A., and Krämer, E., “Trade Study: Influence of Different Blade Shape Designs on Forward Flight and Hovering Performance of an Isolated Rotor,” 37th European Rotorcraft Forum, ERF, 2011.

[2] Kranzinger, P., Hollands, M., Keßler, M., Wagner, S., and Krämer, E., “Generation and Verification of Meshes Used in Automated Process Chains to Optimize Rotor Blades,” 50th AIAA Aerospace Sciences Meeting, Jan. 2012.

[3] Benoit, B., Dequin, A.-M., Kampa, K., von Grünhagen, W., Basset, P.-M., and Gimonet, B., “HOST, A General Helicopter Simulation Tool for Germany and France,” American Helicopter Society, 56th Annual Forum, 2000.

[4] Kroll, N., Eisfeld, B., and Bleecke, H. M., “FLOWer,” *Notes on Numerical Fluid Mechanics*, Vol. 71, 1999, pp. 58–68.

[5] Keßler, M. and Wagner, S., “Source-time Dominant Aeroacoustics,” Computers & Fluids, Vol. 33, No. 5, 2004.

[6] Taguchi, G., Elsayed, E. A., and Hsiang, T., *Quality Engineering in Production Systems*, McGraw-Hill, Singapore, 1989.

[7] Basset, P.-M., Heuze, O., Prasad, J., and Hamers, M., “Finite State Rotor Induced Flow Model For Interferences and Ground Effect,” American Helicopter Society, 57th Annual Forum, 2001.

[8] Jameson, A., “Time Dependent Calculations using Multigrid, with Applications to Unsteady Flows past Airfoils and Wings,” AIAA 10th Computational Fluid Dynamics Conference, 1991.

[9] Wilcox, D. C., *Turbulence Modeling for CFD*, DCW Industries, Inc., München, third edition, 2006.

[10] Benek, J. A., Steger, J. L., Dougherty, F., and Buning, P. G., “Chimera: A grid-embedding technique,” *NASA techdocs*, Paper 19860022770, April 1986, p. 86N32242.

[11] Dietz, M., *Simulation der Umströmung von Hubschrauberkonfigurationen unter Berücksichtigung von Strömungs-Struktur-Kopplung und Trimmung*, PhD thesis, Universität Stuttgart, 2009.

[12] Altmikus, A., Wagner, S., Beaumier, P., and Servera, G., “A Comparison: Weak versus Strong Modular Coupling for Trimmed Aeroelastic Rotor Simulations,” American Helicopter Society, 58th Annual Forum, 2002.

[13] Leishman, J. G., *Principles of Helicopter Aerodynamics*, Cambridge Aerospace Series, second edition, 2006.

[14] Gervais, M. and Gareton, V., “Analysis of Main Rotor Noise Reduction Due to Novel Planform Design - The Blue Edge^{TM} Blade,” 37th European Rotorcraft Forum, ERF, 2011.